ELSEVIER

Buoyancy-assisted flow reversal and convective heat transfer in entrance region of a vertical rectangular duct

Chin-Hsiang Cheng [a,*], Chun-Jen Weng [a], Win Aung [b,1]

[a] *Department of Mechanical Engineering, Tatung University, 40 Chungshan North Road, Sec. 3, Taipei 10451, Taiwan, ROC*
[b] *Division of Engineering Education and Centers, National Science Foundation, Arlington, VA 22230, USA*

Abstract

In this study, predictions of buoyancy-assisted flow reversal and convective heat transfer in the entrance region of a vertical rectangular duct are reported for the first time. In line with the current trend toward the use of computationally efficient numerical methods, the present study is based on the use of a three-dimensional parabolic, boundary-layer model and the FLARE approximation. Physical situations investigated include cases with various asymmetric heating conditions over wide ranges of parameters. Analytical solutions for the fully developed flows are also presented, and the criteria for the flow reversal to occur are predicted. Solutions for the developing flow obtained in this study agree closely with the elliptic-model solutions, and precisely approach the fully developed solutions downstream. © 2000 Elsevier Science Inc. All rights reserved.

Keywords: FLARE; Parabolic model; Flow reversal; Convection

1. Introduction

Mixed convection heat transfer associated with fluid flow in vertical channels is a topic of continuing interest to the researchers owing to relevance to heat exchangers and electronic equipment. A buoyancy-assisted flow reversal phenomenon having profound influence on the flow instabilities and heat transfer in the channels has received attention in a number of recent reports. El-Shaarawi and Sarhan (1980) and Aung and Worku (1986a,b) presented numerical and theoretical solutions for the thermal and flow fields in parallel-plate channels. The criteria for flow reversal to occur can be determined based on the solutions proposed by Aung and Worku (1986b). Cheng and Yang (1994) investigated a similar problem in a channel with a series of fins attached on one channel wall, and evaluated the influence of flow reversal on the heat transfer characteristics of the fins. Iqbal and Aggarwala (1971) presented the analytical solution for fully developed flow in a vertical rectangular duct with an axially constant heat flux condition. More recently, Cheng et al. (1995, 2000) extended the analysis to higher-Grashof-number regime and observed buoyancy-assisted reversed flow.

A number of experimental reports concerned with the buoyancy-assisted reversed flow are available. For example, Morton et al. (1989) performed an experimental study and investigated this phenomenon for laminar pipe flow. Lately, this phenomenon was further studied experimentally by Gau et al. (1992) for the flow in an asymmetrically heated vertical parallel-plate channel.

Note that the nature of the flow in a vertical rectangular duct is inherently three-dimensional. Increasing attention is drawn to three-dimensional flow-reversal problems since the information of three-dimensional flow is important in practical applications. However, physical understanding in three-dimensional flow reversal is still limited because these flows are more complicated to analyze than two-dimensional ones. To the authors' knowledge, the numerical studies performed by Cheng et al. (1995, 2000) comprise the only published reports dealing with three-dimensional buoyancy-assisted mixed convection and separated flow in rectangular ducts.

To investigate internal flows with flow separations, attention is usually given to elliptic-type Navier-Stokes models for numerical computation. However, as shown by many authors, including Ingham et al. (1988), Vasilev (1994), and Cheng et al. (1995), the parabolic-type boundary-layer model coupled with a FLARE approximation has proven to be useful. More recently, direct comparisons between the parabolic and the elliptic models for predicting two-dimensional and three-dimensional flows separations have been performed by Cheng et al. (1997, 2000). A good agreement between the parabolic- and the elliptic-model solutions has been found, and the results also show that the computer time and computation efforts

---

* Corresponding author. Tel.: +886-02-25925252-3410; fax: +886-02-25997142.

E-mail addresses: cheng@ttu.edu.tw (C.-H. Cheng), waung@nsf.gov (W. Aung).

[1] Present address: College of Engineering, Southern Illinois University, Carbondale, IL, USA.

Notation

B	aspect ratio $= y_0/x_0$
g	gravitational acceleration
Gr	Grashof number $= g\beta(T_H - T_L)y_0^3/v^2$
Nu_x	local Nusselt number on wall surfaces at $Y = 0$ or $Y = 1$; see Eq. (8a)
Nu_y	local Nusselt number on wall surfaces at $X = 0$ or $X = 1$; see Eq. (8b)
$\overline{Nu}$	average Nusselt number on wall; see Eqs. (9a) and (9b)
p	cross-sectional pressure
$\bar{p}$	cross-sectional mean pressure
P	dimensionless cross-sectional pressure; see Eq. (2)
$\overline{P}$	dimensionless cross-sectional mean pressure; see Eq. (2)
Pr	Prandtl number
Re	Reynolds number $= w_0 y_0/v$
T	fluid temperature
u, v	transverse velocity components in x- and y-directions

U, V	dimensionless transverse velocity components; see Eq. (2)
w	axial velocity component in z-direction
w_0	average axial velocity
W	dimensionless axial velocity component; see Eq. (2)
x, y, z	rectangular coordinate system
x_0, y_0	length and width of cross-section of duct
X, Y, Z	dimensionless coordinate system; see Eq. (2)

Greeks

α	thermal diffusivity of fluid
β	coefficient of volumetric expansion of fluid
θ	dimensionless fluid temperature; see Eq. (2)
v	kinematic viscosity of fluid
ρ	fluid density

Subscripts

H	hotter wall
L	ambient condition/colder wall
s	separation point

---

required for the parabolic boundary-layer model are at least an order of magnitude less than those for the the elliptic model. The reduction in computer time and efforts is particularly significant for three-dimensional flow analyses.

The FLARE method, first proposed by Reyhner and Flu-gge-Lotz (1968) for the two-dimensional flow analysis, in essence suggests that in the negative-axial-velocity-component regions, the axial convective term $u\partial u/\partial x$ in the two-dimensional boundary layer momentum equation may be represented by $C \mid u \mid \partial u/\partial x$, where C is zero or a small positive constant and u is just the axial velocity component. In this study, the parabolic boundary-layer model and the FLARE approximation is extended and applied to extensively evaluate the effects of heating condition on the flow pattern of three-dimensional buoyancy-assisted flow reversal and heat transfer in a vertical rectangular duct. Physical parameters, including the Prandtl number (Pr), the buoyancy parameter (Gr/Re), and the aspect ratio of the cross-section of the duct (B), are varied in wide ranges. For validation, the elliptic-model solutions for several typical cases are considered. Closed-form solutions for the fully developed flows under various heating conditions are also carried out. Based on the analytical solutions, the criteria for the occurrence of flow reversal for various heating conditions are predicted.

The present study is motivated by the fact that the predominant majority of engineering computations is now carried out on small, stand-alone computers and hence, the search for efficient computation schemes is more relevant than ever.

As shown in Fig. 1, fluid enters a vertical rectangular duct of cross-section area $x_0 \times y_0$ at ambient temperature (T_L) with uniform velocity (w_0). The flow traverses upwards and is heated by the hotter wall at T_H in a buoyancy-assisted situation. Four possible asymmetric heating conditions, namely, Cases a–d, are considered in this study. As shown in Table 1, these four heating conditions include one-wall, two-wall and three-wall heating situations. In certain circumstances, for instance when the heating is sufficiently intense, flow reversal may occur inside the duct. The physical situation shown in Fig. 1 is actually a one-wall heating condition (Case a). The fully developed region is finally reached after a development length; therefore, the numerical solutions for the flow and temperature fields in the entrance region should in principle approach asymptotically the fully developed solutions downstream.
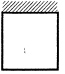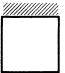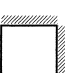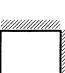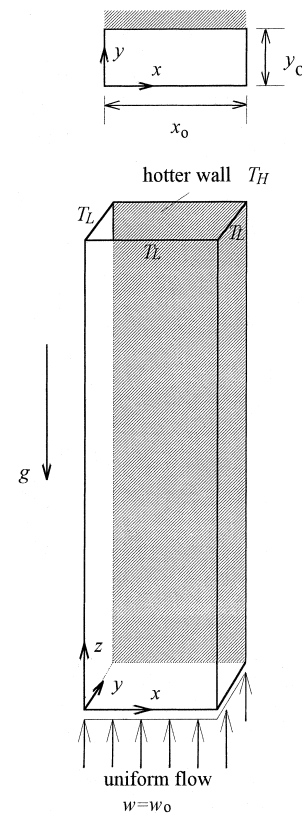

Fig. 1. A vertical rectangular duct with one-wall heating (Case a).

2. Theoretical analysis

The flow is considered to be steady and laminar. The fluid properties are assumed to be constant except for the density in the buoyancy term of the momentum equation for the vertical direction. The mathematical formulation of three-dimensional, boundary-layer model for a Boussinesq fluid is expressed in dimensionless vector form as

Table 1
Heating conditions

case	heating condition
a	one-wall heating
b	two-wall heating
c	two-wall heating
d	three-wall heating

$$\overline{\nabla} \cdot \vec{V} = -\frac{\partial W}{\partial Z}, \tag{1}$$

$$\overline{\nabla} \cdot (\vec{V}U - \overline{\nabla}U) = -\frac{\partial P}{\partial X} - \frac{\partial(WU)}{\partial Z}, \tag{2}$$

$$\overline{\nabla} \cdot (\vec{V}V - \overline{\nabla}V) = -\frac{\partial P}{\partial Y} - \frac{\partial(WV)}{\partial Z}, \tag{3}$$

$$\overline{\nabla} \cdot (\vec{V}W - \overline{\nabla}W) = -\frac{\mathrm{d}\overline{P}}{\mathrm{d}Z} + \frac{Gr}{Re}\theta - \left[C \mid W \mid \frac{\partial W}{\partial Z} - W\frac{\partial W}{\partial Z}\right] - \frac{\partial W^2}{\partial Z}, \tag{4}$$

$$\overline{\nabla} \cdot \left(\vec{V}\theta - \frac{1}{Pr}\overline{\nabla}\theta\right) = -\left[C \mid W \mid \frac{\partial \theta}{\partial Z} - W\frac{\partial \theta}{\partial Z}\right] - \frac{\partial(W\theta)}{\partial Z}, \tag{5}$$

where the cross-sectional velocity vector ($\vec{V}$) and the operator ($\overline{\nabla}$) are defined by $\vec{V} = U\vec{i} + V\vec{j}$ and $\overline{\nabla} = (\partial/\partial X)\vec{i} + (\partial/\partial Y)\vec{j}$, respectively.

These above dimensionless parameters have been defined as

$X = x/x_0, \quad Y = y/y_0, \quad Z = z/(y_0 Re), \quad B = y_0/x_0,$

$U = uy_0^2/(vx_0), \quad V = vy_0/v, \quad W = w/w_0, \quad P = py_0^2/(\rho v^2),$

$\overline{P} = (\bar{p} - p_L)/(\rho w_0^2), \quad \theta = (T - T_L)/(T_H - T_L). \tag{6}$

In the above, p_L is the ambient pressure, and $\mathrm{d}\overline{P}/\mathrm{d}Z$ is the streamwise gradient of the dimensionless mean pressure.

The terms in the parentheses on the right-hand side of Eqs. (4) and (5) are introduced by the FLARE method. The value C is assigned to be zero or a small value at the nodal points of computation with $W < 0$. Thus, the magnitude of the axial convective term is artificially adjusted with the constant C for the negative-W areas. However, for points with $W > 0$, C is set equal to 1.0; therefore, for these points the terms in the parentheses on the right-hand side of Eqs. (4) and (5) vanish.

Boundary conditions at the inlet can be written as

$$U = V = 0, \quad W = 1, \quad \overline{P} = 0, \quad \theta = 0 \quad \text{at} \quad Z = 0. \tag{7}$$

On the other hand, on the solid walls, the no-slip condition is specified for all velocity components. For the heated walls, the value of θ is equal to unity, while for the lower-temperature walls, $\theta = 0$.

3. Numerical solutions for developing flows

The computation for the developing region starts from the inlet at $Z = 0$, and then is advanced continuously in the axial direction. By following this axial marching procedure, the solutions at each cross-section are obtained by using the known values at the previous cross-section. When the fully developed flow region is reached, the computation is terminated.

The axial pressure gradient $\mathrm{d}\overline{P}/\mathrm{d}Z$ is adjusted iteratively to make axial velocity profile $W(X, Y, Z)$ satisfy the overall mass conservation at each cross-section, as described by Patankar and Spalding (1972) and Ramakrishna et al. (1982). When reversed flow occurs, however, some modifications for the iteration scheme are required. Further information about these solution methods is provided by Cheng et al. (2000).

3.1. Flow and temperature fields

Fig. 2 shows the distributions of axial velocity component (W) at different axial locations by using the contour lines, at $B = 0.5$, $Gr/Re = 100$, and $Pr = 0.71$, under various heating conditions. The shaded walls indicate the heated walls. It is noticed that the fluid near the hotter walls is accelerated by the buoyancy force. Consequently, the reversed flow is first found at corners adjacent to the cold walls. The reversed flow grows gradually in axial direction and then occupies an extent of the low-temperature zone. In this particular situation, it is obvious that Cases c and d result in stronger reversed flows than Cases a and b.

Fig. 3 displays the development of axial velocity component, temperature distribution (θ), and transverse flow pattern, for a square duct ($B = 1$) under heating condition Case c, at $Gr/Re = 200$ and $Pr = 0.71$. The temperature field is indicated by the isothermal lines and the transverse flow pattern is illustrated with the cross-sectional velocity vectors formed by transverse velocity components U and V. The movement of the fluid toward the hotter walls is clearly observed from the transverse velocity vector plots. However, these transverse velocity components of flow diminish rapidly as the fluid goes downstream. The development of the thermal boundary layers on the hotter walls can also be observed in this figure. Note that a pure-diffusion thermal field is asymptotically established at $Z \to \infty$.

Effects of Prandtl number on the development of the axial velocity and temperature profiles at the middle plane ($X = 1/2$), for $B = 1$ and $Gr/Re = 300$ under heating condition of Case a are shown in Fig. 4. The data of W and θ at different axial locations are provided. The Prandtl number is assigned to be 0.71, 4 and 7. It is clear that the negative-velocity area appears at a location closer to the inlet for the fluid with lower Prandtl number. On the other hand, lower Prandtl number causes a thicker thermal boundary layer in the developing region so as to reduce the local heat transfer rate on the hotter wall. It is noticed that the curves of W and θ at
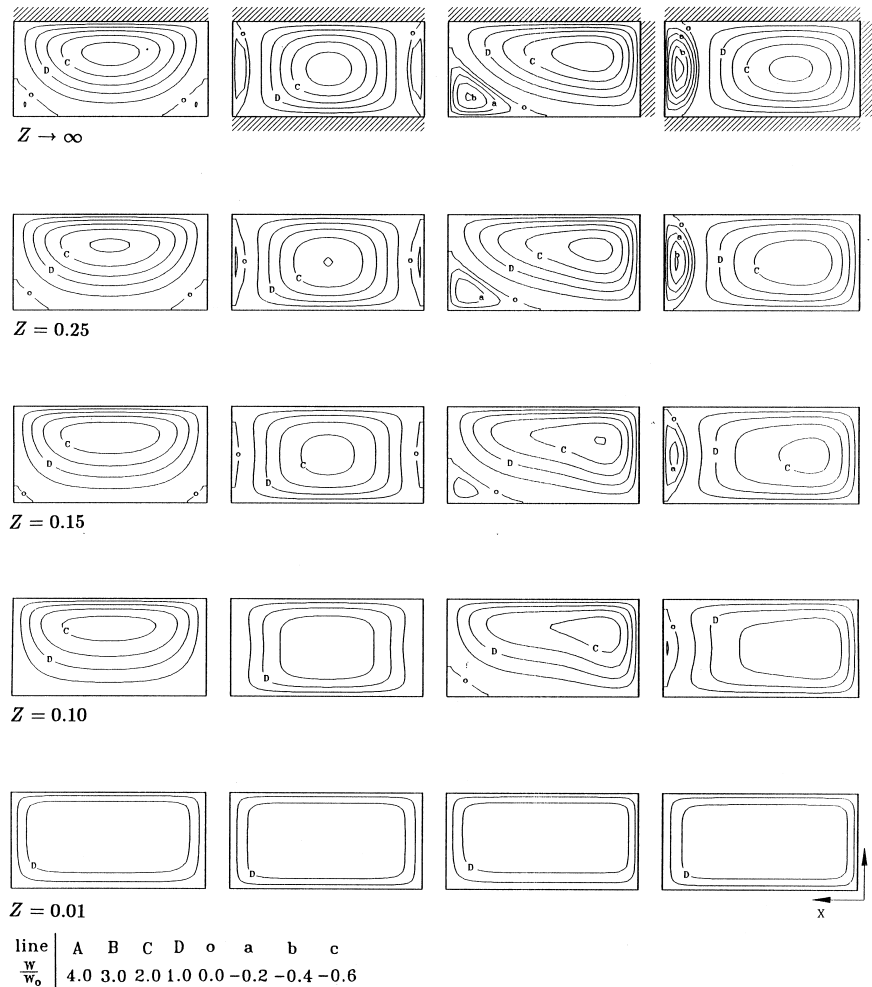
line	A	B	C	D	o	a	b	c
$\dfrac{W}{W_o}$	4.0	3.0	2.0	1.0	0.0	−0.2	−0.4	−0.6

Fig. 2. Developing axial velocity distributions (W) at $B = 0.5$, $Gr/Re = 100$, and $Pr = 0.71$, under various heating conditions.

$Z \to \infty$ exactly approach the analytical solutions for the fully developed flow, which will be discussed later. Also notice that the fully developed velocity and temperature profiles are independent of the Prandtl number.

Attention is now drawn to the location of separation point (Z_s). Table 2 shows the dependence of Z_s on the parameters Pr, B, and Gr/Re, for the one-wall heating situation, Case a. It is found that the separation point appears at a location closer to the inlet for the fluid with lower Prandtl number. Meanwhile, as the value of B is elevated, the threshold value of Gr/Re for separation to occur is increased.

3.2. Pressure variation and heat transfer

Variation of the cross-sectional mean pressure in z-direction is shown in Fig. 5. In Fig. 5(a), the heating condition effect is evaluated at $B = 1$, $Gr/Re = 200$ and $Pr = 0.71$. It is found that $-\overline{P}$ achieves a maximum value within the duct, and an adverse pressure gradient is formed downstream. The adverse pressure gradient is a driving force that leads to the reversed flow. The influence of buoyancy on the pressure variation is shown in Fig. 5(b), at $B = 1$ and $Pr = 0.71$ under the same heating condition Case c.

The solutions for temperature distribution are used to calculate the local heat transfer rates on the walls. Local Nusselt number, Nu_x, denoting the dimensionless local heat flux on the wall at $Y = 0$ or $Y = 1$ is defined by

$$Nu_x = \left| \frac{y_0}{T_H - T_L} \frac{\partial T}{\partial y} \right| = \left| \frac{\partial \theta}{\partial Y} \right|. \tag{8a}$$

Similarly, local Nusselt number on wall at $X = 0$ or $X = 1$, Nu_y, is given by

$$Nu_y = \left| \frac{y_0}{T_H - T_L} \frac{\partial T}{\partial x} \right| = B \cdot \left| \frac{\partial \theta}{\partial X} \right|. \tag{8b}$$

Nu_x and Nu_y are functions of X and Y along the wall surface, respectively, and may be calculated at each cross-section in z-direction. Integration of Nu_x and Nu_y yields the average wall Nusselt numbers on the walls. That is,

$$\overline{Nu} = \frac{1}{x_0} \int_0^{x_0} \left| \frac{y_0}{T_H - T_L} \frac{\partial T}{\partial y} \right| dx = \int_0^1 Nu_x \, dX \tag{9a}$$

for walls at $Y = 0$ and $Y = 1$. And similarly,

$$\overline{Nu} = \frac{1}{y_0} \int_0^{y_0} \left| \frac{y_0}{T_H - T_L} \frac{\partial T}{\partial x} \right| dy = \int_0^1 Nu_y \, dY \tag{9b}$$

for walls at $X = 0$ and $X = 1$. Data of $\overline{Nu}$ at different cross-sections indicate the axial variation of heat transfer on the walls.

Distributions of local Nusselt numbers on all the four walls, determined by equations (8a) and (8b), and their variation in z-direction are shown in Fig. 6. In this figure, the case with $B = 1$, $Gr/Re = 200$ and $Pr = 0.71$ under heating condition
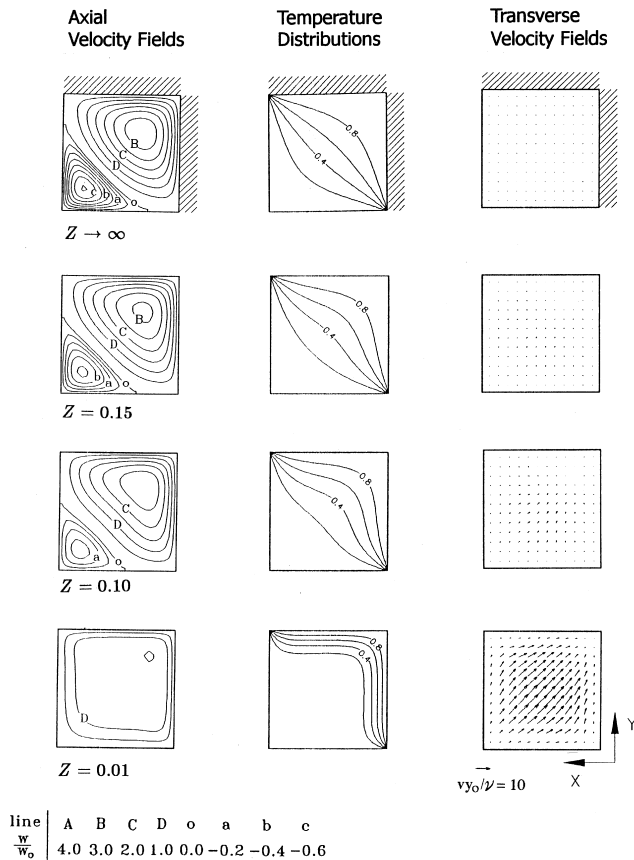
Axial
Velocity Fields

Temperature
Distributions

Transverse
Velocity Fields

$Z \to \infty$

$Z = 0.15$

$Z = 0.10$

$Z = 0.01$

$\overrightarrow{vy_o/\nu} = 10$

line	A	B	C	D	o	a	b	c
$\frac{W}{W_o}$	4.0	3.0	2.0	1.0	0.0	−0.2	−0.4	−0.6

Fig. 3. Development of axial velocity distribution (W), transverse flow pattern (vectors formed by U and V), and temperature distribution (θ) at $B = 1$, $Gr/Re = 200$, and $Pr = 0.71$, for Case c.

Case d is investigated. For each of the four walls, highest local Nusselt numbers are found at the inlet, and the Nusselt numbers asymptotically approach minimum values at $Z \to \infty$.

Fig. 7 shows the effects of Gr/Re and Pr on the average Nusselt number ($\overline{Nu}$) on the wall at $Y = 1$ for $B = 2$ under heating condition Case a. Notice that under Case a, only the wall at $Y = 1$ is heated. In Fig. 7(a), Pr is fixed at 0.71, whereas the value of Gr/Re is varied. It is obvious that the average Nusselt number on the heated wall increases with Gr/Re, but assumes a minimum, asymptotic value in the fully developed regime. On the other hand, the Prandtl number of fluid is changed in Fig. 7(b), with Gr/Re fixed at 900, to evaluate the Prandtl number effect. This figure reveals clearly that heat transfer is appreciably increased as the Prandtl number is elevated.

Variations of average Nusselt number in the axial direction, at $B = 1$, $Gr/Re = 200$ and $Pr = 0.71$, under various heating conditions are shown in Fig. 8. Values of all the four walls for each heating condition are displayed. The solid and the dashed lines shown in this figure indicate the data of hotter and colder walls, respectively. Note that in Cases a–c, the hotter walls always exhibit higher heat transfer rates than the colder walls. However, for condition Case d, a three-wall heating situation, the average Nusselt numbers of the three hotter walls are obviously lower than those of the colder wall.

3.3. Verifications by elliptic-model solutions

The accuracy of numerical solutions obtained by FLARE approximation is demonstrated by comparison with the
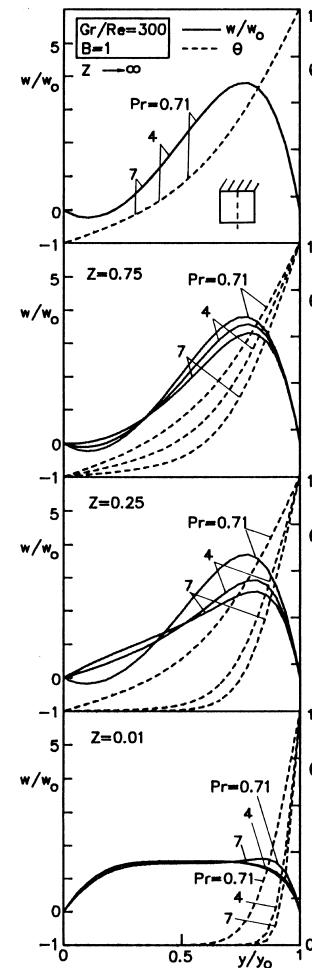
Fig. 4. Effect of Prandtl number on the development of axial velocity and temperature profiles at the middle plane ($X = 1/2$), at $B = 1$ and $Gr/Re = 300$, for Case a.

Table 2
Effects of Pr, B, and Gr/Re on the location of separation point, for Case a

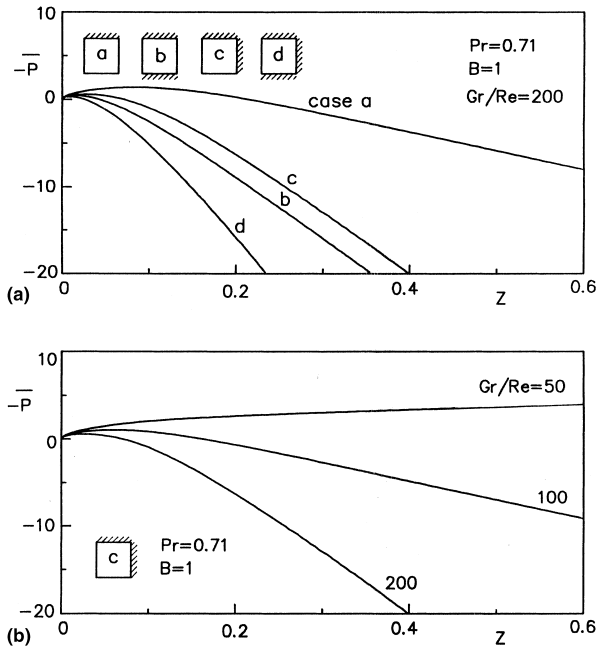| Pr	B	Gr/Re	Z_s
0.71	0.5	50	*
		100	0.107
		150	0.072
	1.0	100	*
		200	0.112
		300	0.077
	2.0	600	*
		700	0.157
		900	0.097
4.0	0.5	50	*
		100	0.467
		150	0.287
	1.0	100	*
		200	0.462
		300	0.282
	2.0	600	*
		700	0.587
		900	0.337

* No reversal.

Fig. 5. Variation of mean pressure in axial direction: (a) heating condition effect, at $B = 1$, $Gr/Re = 200$, and $Pr = 0.71$; (b) buoyancy effect, at $B = 1$ and $Pr = 0.71$, for Case c.
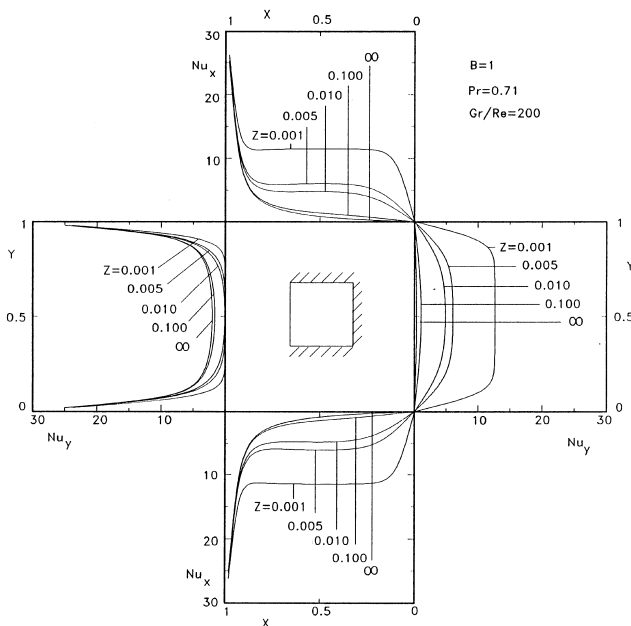

Fig. 6. Distributions of local Nusselt numbers on the four wall surfaces and their variation in axial direction at $B = 1$, $Gr/Re = 200$, and $Pr = 0.71$, for Case d.

corresponding elliptic-model solutions. The elliptic model includes the elliptic-type full Navier-Stokes equations and energy equation. Computations have been carried out on a staggered grid system with $26 \times 26 \times 101$ grids in the $x \times y \times z$ directions. Equal grid sizes are used for both elliptic and parabolic models. More information related to the validation of the parabolic model has been reported in (Cheng et al., 2000). Therefore, detailed descriptions about the governing equations and the numerical methods are not repeated here.
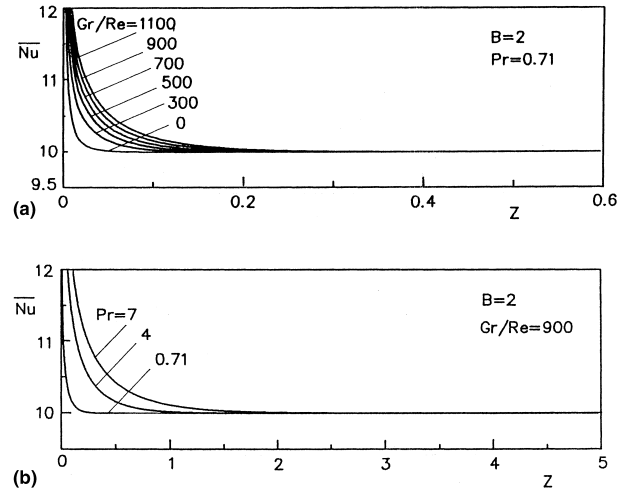

Fig. 7. Variation of average Nusselt number ($\overline{Nu}$) on the heated wall under Case a, for $B = 2$: (a) effect of Gr/Re, at $Pr = 0.71$; (b) effect of Pr, at $Gr/Re = 900$.
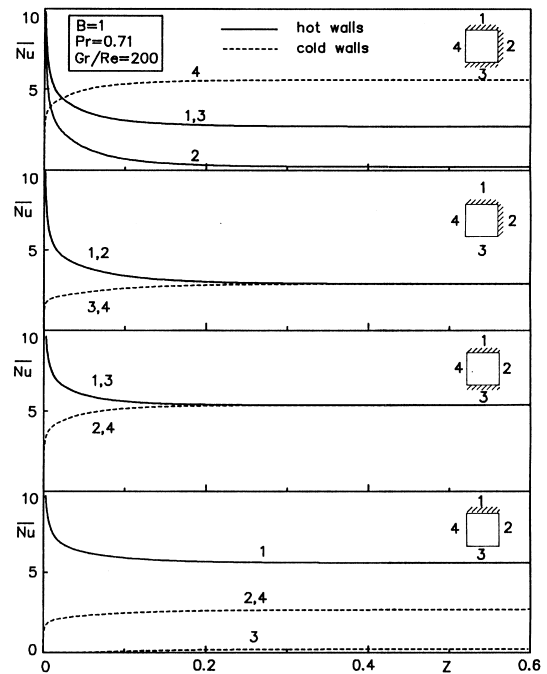

Fig. 8. Variation of average Nusselt number ($\overline{Nu}$) on the walls under various heating conditions, at $B = 1$, $Gr/Re = 200$, and $Pr = 0.71$.

Presented in the left and the right plots of Fig. 9 are the cross-sectional distributions of axial velocity component (W) predicted by the parabolic and the elliptic models, respectively. The flow is subject to heating condition Case a and at $B = 1$, $Gr/Re = 300$, and $Pr = 0.71$. In Fig. 9, visual inspection shows that the solutions obtained by FLARE approximation agree closely with the elliptic-model solutions.

The comparison in the variation of dimensionless pressure along streamwise direction under various heating conditions, at $B = 1$, and $Gr/Re = 200$, is shown in Fig. 10. The data of dimensionless cross-sectional mean pressure ($\overline{P}$) are plotted in this figure. On the other hand, the values on the centerline ($x/x_0 = 1/2$, $y/y_0 = 1/2$) predicted by the elliptic model are
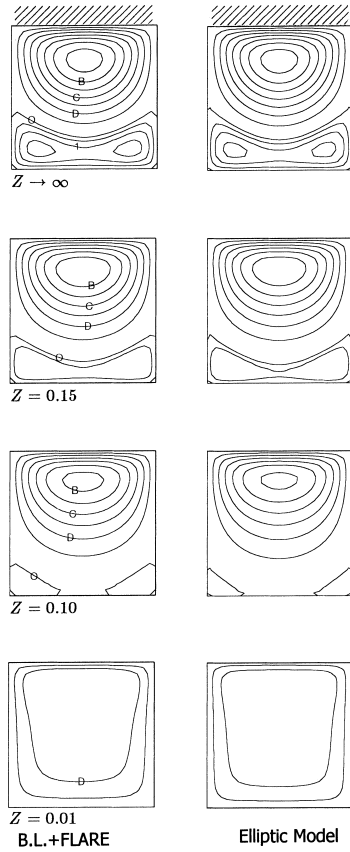
Fig. 9. Cross-sectional distributions of axial velocity component (W) under Case a: comparison between the parabolic and the elliptic models, at $B = 1$, $Gr/Re = 300$, and $Pr = 0.71$.

taken to represent the elliptic-model results. Agreement between these two sets of data is again found.

3.4. Fully developed flows

In theory, the flow reaches fully developed region after a sufficient distance from the inlet. When this region is approached, the distribution of axial velocity component $W(X, Y, Z)$ of the flow becomes invariant in z-direction as the transverse velocity components, $U(X, Y, Z)$ and $V(X, Y, Z)$, diminish gradually. A pure-diffusion temperature field, which is independent of the Prandtl number and the main stream strength, will also be asymptotically developed.

Eqs. (4) and (5) can then be readily reduced to the fully developed flow equations according to the physical features stated above. The obtained equations are solved by means of the method of separation of variables and a superposition technique. The solutions for W under various heating conditions are carried out as
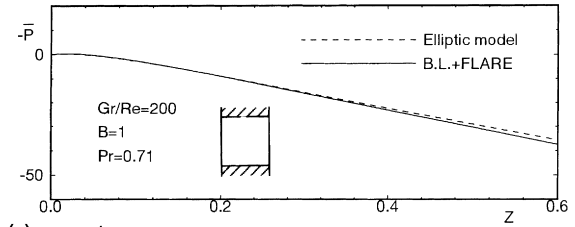
Case a.

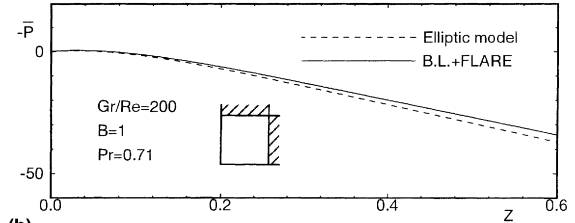$$W = W_p + W_{\theta 1}, \tag{10a}$$

Case b.

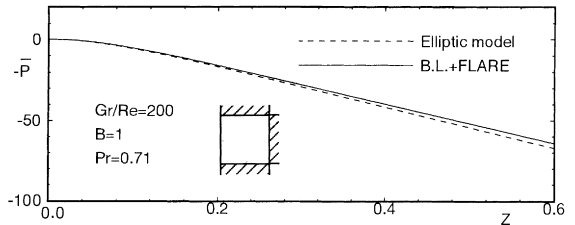$$W = W_p + W_{\theta 1} + W_{\theta 2}, \tag{10b}$$

Case c.

$$W = W_p + W_{\theta 1} + W_{\theta 3}, \tag{10c}$$

Fig. 10. Variations of dimensionless pressure along streamwise direction under various heating conditions, comparison between the parabolic and the elliptic models at $B = 1$, and $Gr/Re = 200$.

Case d.

$$W = W_p + W_{\theta 1} + W_{\theta 2} + W_{\theta 3}, \tag{10d}$$

where

$$W_p(X, Y) = \frac{d\overline{P}}{dZ}\left[\frac{1}{2B^2}(X^2 - X) + \overline{W}_p(X, Y)\right] \tag{11a}$$

$$W_{\theta_i}(X, Y) = \sum_{m=1}^{\infty} K_{mi}(Y)\sin(m\pi X), \quad i = 1, 2, 3 \tag{11b}$$

and

$$\overline{W}_p(X, Y) = \left(\frac{4}{B^2\pi^3}\right)\sum_{m=1}^{\infty}$$
$$\times \left[\frac{\sinh\left((2m-1)\pi B(1-Y)\right) + \sinh\left((2m-1)\pi BY\right)}{\sinh\left((2m-1)\pi B\right)}\right]$$
$$\times \left[\frac{\sin\left((2m-1)\pi X\right)}{(2m-1)^3}\right], \tag{12a}$$

$$K_{m1}(Y) = \frac{G_m}{2m\pi B \sinh(m\pi B)}\frac{Gr}{Re}$$
$$\times \left[-Y\cosh(m\pi BY) + \frac{\cosh(m\pi B)\sinh(m\pi BY)}{\sinh(m\pi B)}\right], \tag{12b}$$

$$K_{m2}(Y) = \frac{G_m}{2m\pi B \cdot \sinh(m\pi B)}\frac{Gr}{Re}$$
$$\times \left[Y\cosh\left(m\pi B(1-Y)\right) - \frac{\sinh(m\pi BY)}{\sinh(m\pi B)}\right], \tag{12c}$$

$$K_{m3}(X) = \frac{G_m}{\left(\frac{2m\pi}{B}\right) \cdot B^2 \cdot \sinh\left(\frac{m\pi}{B}\right)} \frac{Gr}{Re}$$

$$\times \left[X \cosh\left(\frac{m\pi}{B}(1-X)\right) - \frac{\sinh\left(\frac{m\pi X}{B}\right)}{\sinh\left(\frac{m\pi}{B}\right)} \right]. \qquad (12d)$$

Meanwhile, the solutions for temperature distributions for the fully developed flows are

Case a.

$$\theta = \theta_1, \qquad (13a)$$

Case b.

$$\theta = \theta_1 + \theta_2, \qquad (13b)$$

Case c.

$$\theta = \theta_1 + \theta_3, \qquad (13c)$$

Case d.

$$\theta = \theta_1 + \theta_2 + \theta_3, \qquad (13d)$$

where

$$\theta_1 = \sum_{m=1}^{\infty} G_m \frac{\sinh(m\pi B Y)}{\sinh(m\pi B)} \sin(m\pi X) \qquad (14a)$$

$$\theta_2 = \sum_{m=1}^{\infty} G_m \frac{\sinh\left(m\pi B(1-Y)\right)}{\sinh(m\pi B)} \sin(m\pi X) \qquad (14b)$$

$$\theta_3 = \sum_{m=1}^{\infty} G_m \frac{\sinh\left(\frac{m\pi}{B}(1-X)\right)}{\sinh\left(\frac{m\pi}{B}\right)} \sin(m\pi Y) \qquad (14c)$$

and

$$G_m = 2[1 - (-1)^m]/m\pi. \qquad (14d)$$

Comparison between the numerical predictions and the analytical solutions for the axial velocity distribution of the fully developed flows is shown in Table 3 for several typical cases. The numerical solutions for the developing flows precisely approach the fully developed solutions downstream.

In this study, the main stream moves upward; however, as flow reversal takes place, a descending plume is formed along the surfaces of the colder walls. The bi-directional fluid motion inside the duct may lead to flow instability. In that case, a significant change in heat transfer behavior may be caused by the flow reversal, and hence, prediction of the occurrence of the flow reversal is relevant to the thermal management for the related systems. Therefore, of particular interest is the criterion for flow reversal to occur. The above velocity solutions reflect the influence of the buoyancy parameter Gr/Re and the aspect ratio B on the flow pattern. Calculated with these equations, the parameter zones in which the reversed flow may take place are predicted and shown in Fig. 11. In this figure, the hatched curves indicate the critical lines for the flow reversal to occur. For each heating condition, when the value of B is fixed, the flow reversal takes place as long as the ratio Gr/Re exceeds a threshold value. If the values of B is elevated, the threshold value of Gr/Re is increased. This is consistent with the results given in Table 2. The threshold values may be different for different heating conditions. In general, it is lower for Case c than for the other three cases. This implies that under the heating condition Case c, flow reversal is more likely to take place.

Table 3
Comparison between numerical and analytical solutions for the fully developed flows, at $B = 1$ and $Pr = 0.71$

Case	Analytical (Fully-Developed Flow)	Numerical (Developing Flow)
case a Gr/Re=350		
case b Gr/Re=300		
case c Gr/Re=200		
case d Gr/Re=200		

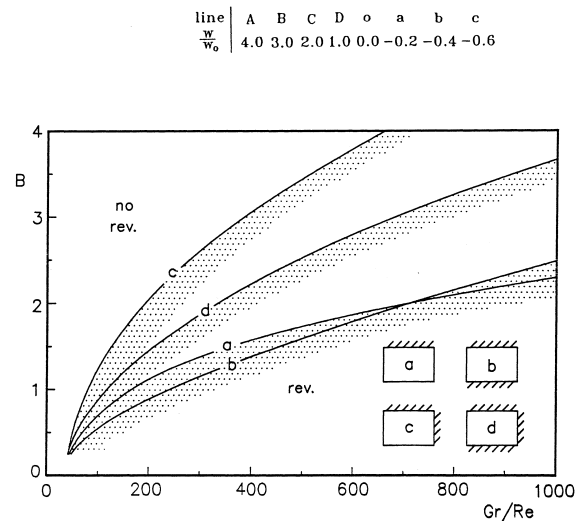| line	A	B	C	D	o	a	b	c
$\frac{W}{W_o}$	4.0	3.0	2.0	1.0	0.0	−0.2	−0.4	−0.6

Fig. 11. Reversed flow zones for various heating conditions.

4. Concluding remarks

The buoyancy-induced three-dimensional flow reversal and heat transfer in the entrance region of a vertical rectangular ducts have been studied numerically. Parabolic boundary-layer model and the FLARE approximation are adopted to predict the flow and thermal fields. Meanwhile, analytical solutions for the fully developed flows under various heating

conditions are presented, and the criteria for the flow reversal to occur are given based on the fully developed flow solutions.

It is found that the strength and the extent of the reversed flow are dependent on the buoyancy parameter Gr/Re, the cross-sectional aspect ratio B, and the Prandtl number Pr. At a fixed value of B, the flow reversal takes place when the ratio Gr/Re exceeds a threshold value. The threshold value is a function of the physical parameters and the heating condition. In this study, four possible asymmetric heating conditions (Cases a–d) are considered. The threshold value is lower for Case c than for the other three cases. In general, the threshold value increases with the aspect ratio B.

The point of separation is found to be closer to the inlet for the fluid with a lower Prandtl number. Furthermore, a lower Prandtl number leads to a thicker thermal boundary layer in the entrance region and hence, reduces the local heat transfer rate on the walls.

Numerical solutions for the developing flow obtained in this study agree closely with the elliptic-model solutions, and precisely approach the fully developed solutions downstream.

Acknowledgements

References

Aung, W., Worku, G., 1986a. Developing flow and flow reversal in a vertical channel with asymmetric wall temperatures. ASME J. Heat Transfer 108, 299–304.

Aung, W., Worku, G., 1986b. Theory of fully developed combined convection including flow reversal. ASME J. Heat Transfer 108, 455–458.

Cheng, C.H., Yang, J.J., 1994. Buoyancy-induced recirculation bubbles and heat convection of developing flow in vertical channels with fin arrays. Int. J. Heat and Fluid Flow 5, 11–19.

Cheng, C.H., Weng, C.J., Aung, W., 1995. Buoyancy effect on the flow reversal on three-dimensional developing flow in a vertical rectangular duct – a parabolic model solution. ASME J. Heat Transfer 117, 238–241.

Cheng, C.H., Huang, S.Y., Aung, W., 1997. Enhancement of FLARE method for predicting buoyancy-induced flow reversal in vertical ducts via parabolic model. Numer. Heat Transfer Part B 31, 327–345.

Cheng, C.H., Lin, C.L., Aung, W., 2000. Predictions of developing flow with buoyancy-assisted flow separation in a vertical rectangular duct: parabolic model versus elliptic model. Numer. Heat Transfer, to appear.

El-Shaarawi, M.A.I., Sarhan, A., 1980. Free convection effects on the developing laminar flow in vertical concentric annuli. ASME J. Heat Transfer 102, 617–622.

Gau, C., Yih, K.A., Aung, W., 1992. Reversed flow structure and heat transfer measurements for buoyancy assisted convection in a heated vertical duct. ASME J. Heat Transfer 114, 928–935.

Ingham, D.B., Keen, D.J., Heggs, P.J., 1988. Flow in vertical channels with asymmetic wall temperature and including situations where reverse flow occur. ASME J. Heat Transfer 110, 910–917.

Iqbal, M., Aggarwala, B.D., 1971. Combined free and forced convection through vertical rectangular channels with unequal heating from sides. J. Appl. Mech. 38, 829–833.

Morton, B., Ingham, D.B., Keen, D.J., Heggs, P.J., 1989. Recirculating combined convection in laminar pipe flow. ASME J. Heat Transfer 111, 106–113.

Patankar, S.V., Spalding, D.B., 1972. A calculation procedure for heat mass and momentum transfer in three-dimensional parabolic flows. Int. J. Heat Mass Transfer 15, 1787–1806.

Ramakrishna, K., Rubin, S.G., Khosla, P.K., 1982. Laminar natural convection along vertical square ducts. Numer. Heat Transfer 5, 59–79.

Reyhner, T.A., Flugge-Lotz, I., 1968. The interaction of a shock wave with a laminar boundary layer. Int. J. Non-linear Mech. 3, 173–199.

Vasilev, V.I., 1994. Computation of separated duct flows using the boundary-layer equations. AIAA J. 32, 1191–1199.